



**HAL**  
open science

# Automatic Ferroelectric Domain Pattern Recognition Based on the Analysis of Localized Nonlinear Optical Responses Assisted by Machine Learning

Boris Croes, Iaroslav Gaponenko, Cédric Voulot, Olivier Grégut, Kokou D Dorkenoo, Fabien Cheynis, Stefano Curiotto, Pierre Müller, Frédéric Leroy, Kumara Cordero-edwards, et al.

► **To cite this version:**

Boris Croes, Iaroslav Gaponenko, Cédric Voulot, Olivier Grégut, Kokou D Dorkenoo, et al.. Automatic Ferroelectric Domain Pattern Recognition Based on the Analysis of Localized Nonlinear Optical Responses Assisted by Machine Learning. *Advanced Physics Research*, 2022, pp.2200037. 10.1002/apxr.202200037 . hal-03899940

**HAL Id: hal-03899940**

<https://hal.science/hal-03899940v1>

Submitted on 15 Dec 2022

**HAL** is a multi-disciplinary open access archive for the deposit and dissemination of scientific research documents, whether they are published or not. The documents may come from teaching and research institutions in France or abroad, or from public or private research centers.

L'archive ouverte pluridisciplinaire **HAL**, est destinée au dépôt et à la diffusion de documents scientifiques de niveau recherche, publiés ou non, émanant des établissements d'enseignement et de recherche français ou étrangers, des laboratoires publics ou privés.



Distributed under a Creative Commons Attribution 4.0 International License

# Automatic Ferroelectric Domain Pattern Recognition Based on the Analysis of Localized Nonlinear Optical Responses Assisted by Machine Learning

Boris Croes, Iaroslav Gaponenko, Cédric Voulot, Olivier Grégut, Kokou D. Dorkenoo, Fabien Cheynis, Stefano Curiotto, Pierre Müller, Frédéric Leroy, Kumara Cordero-Edwards, Patrycja Paruch, and Salia Cherifi-Hertel\*

Second-harmonic generation (SHG) is a nonlinear optical method allowing the study of the local structure, symmetry, and ferroic order in noncentrosymmetric materials such as ferroelectrics. The combination of SHG microscopy with local polarization analysis is particularly efficient for deriving the local polarization orientation. This, however, entails the use of tedious and time-consuming modeling methods of nonlinear optical emission. Moreover, extracting the complex domain structures often observed in thin films requires a pixel-by-pixel analysis and the fitting of numerous polar plots to ascribe a polarization angle to each pixel. Here, the domain structure of GeTe films is studied using SHG polarimetry assisted by machine learning. The method is applied to two film thicknesses: A thick film containing large domains visible in SHG images, and a thin film in which the domains' size is below the SHG resolution limit. Machine learning-assisted methods show that both samples exhibit four domain variants of the same type. This result is confirmed in the case of the thick film, both by the manual pixel-by-pixel analysis and by using piezoresponse force microscopy. The proposed approach foreshows new prospects for optical studies by enabling enhanced sensitivity and high throughput analysis.

## 1. Introduction

Ferroic materials are, in essence, functional materials owing to the switchable character of their ferroic order under external fields. The domain structure formed by the arrangement of the local order parameter at the nano and mesoscale is of the highest importance since it controls the functional properties of these materials.<sup>[1]</sup> For instance, a nonlinear optical crystal can be designed through the periodic arrangement of the polarization in a ferroelectric material, where the domain period controls the wavelength of the photonic crystal.<sup>[2]</sup> The domain boundary regions can also present extraordinary properties different from that of the adjacent domains, which further increase the functionality of the material.<sup>[3]</sup>

Advanced imaging methods are required to study domain configurations in ferroelectric materials due to their reduced size and the complexity of the


domain structure. Modern aberration-corrected transmission electron microscopy (TEM) is undeniably the most suitable technique for resolving complex polarization textures such as vortices,<sup>[4,5]</sup> polar waves,<sup>[6]</sup> or chiral wall arrangements.<sup>[7]</sup> Nevertheless, this method cannot be applied routinely since the sample preparation for TEM measurements is usually difficult, time-consuming, and invasive. Moreover, the obtained information is limited to a small area, which may not represent the overall sample properties.

Piezoresponse force microscopy (PFM) can, to some extent, present a good alternative.<sup>[8]</sup> In particular, vector PFM provides a 3D mapping of the polarization<sup>[9]</sup> that could allow for a detailed description of the domain structure. Despite its essential importance in probing ferroelectric domains, PFM can present a few downsides that hinder its application in some systems. Among these, the need for a base electrode for the measurements, the strong interaction between the probe-sample requires in some cases precise modeling of such interaction, and it is difficult to distinguish between small piezoelectric responses

B. Croes, C. Voulot, O. Grégut, K. D. Dorkenoo, S. Cherifi-Hertel  
 Université de Strasbourg  
 CNRS, IPCMS, UMR 7504, Strasbourg 67000, France  
 E-mail: Salia.Cherifi@ipcms.unistra.fr

I. Gaponenko, K. Cordero-Edwards, P. Paruch  
 DQMP  
 University of Geneva  
 Geneva 1211, Switzerland

F. Cheynis, S. Curiotto, P. Müller, F. Leroy  
 Aix Marseille Université  
 CNRS, CINAM, AMUTECH, Marseille 13288, France

 The ORCID identification number(s) for the author(s) of this article can be found under <https://doi.org/10.1002/apxr.202200037>

© 2022 The Authors. Advanced Physics Research published by Wiley-VCH GmbH. This is an open access article under the terms of the Creative Commons Attribution License, which permits use, distribution and reproduction in any medium, provided the original work is properly cited.

DOI: 10.1002/apxr.202200037

and possible electromechanical deformations induced by non-piezoelectric phenomena such as electrostatic or electrochemical effects.

Low energy electron microscopy and X-ray photoemission electron microscopy allow for a non-contact and non-invasive observation of polar domain structures with a lateral resolution better than 50 nm as demonstrated in BiFeO<sub>3</sub> thin films.<sup>[10]</sup> On the other hand, these methods are surface sensitive and require a thorough treatment of the sample in ultrahigh vacuum conditions before the measurements to reduce surface contamination and external charge screening that can strongly affect the quality of the detected signal.

In contrast to this, optical studies are user-friendly, and no substantial sample preparation is required. While optical methods are generally shunned due to their limited lateral resolution, their combination with advanced data analysis methods has recently extended their capability by multiplying their resolving power. Principal component analysis has proven its efficiency in capturing Raman signatures of ferroic domain walls in LiNbO<sub>3</sub> single crystals<sup>[11]</sup> in spite of their sub-10 nm scale. The recent development of open-source algorithms based on artificial intelligence has further impacted the development of contemporary Raman and surface-enhanced Raman scattering sensors.<sup>[12]</sup> Similarly, machine learning methods have boosted the sensitivity of second-harmonic generation microscopy (SHG) to obtain phase information in reference-free experiments,<sup>[13]</sup> provide automatic cancer diagnosis in breast tissues using high-throughput SHG polarimetry studies,<sup>[14]</sup> or achieve correlative imaging at the nanoscale by combining SHG polarimetry and scanning probe microscopy.<sup>[15]</sup>

This study demonstrates the high potential of laterally-resolved SHG polarimetry assisted by machine learning methods to investigate the ferroic order through the analysis of the domain structure of Germanium Telluride (GeTe), a high-*T<sub>c</sub>* non-oxide ferroelectric. Such Rashba-type ferroelectrics have recently attracted great attention owing to their potential technological applications based on the ferroelectric control of the Rashba-type spin-orbit coupling.<sup>[16–18]</sup> Even if the ferroelectricity of crystalline  $\alpha$ -GeTe is well-established, little is known about the domain structure of epitaxial GeTe films and its effect on the functionality of the material. Here, we study the domain structure of GeTe thin films epitaxially grown on Si(111). The coexistence of four different domain variants is demonstrated: the main c-domain with out-of-plane polarization and a-domains forming nano-stripes oriented along three different orientations and exhibiting an in-plane polarization along their short axis (see **Figure 1**). The local polarization orientation of each domain is derived using SHG microscopy and pixel-by-pixel polarization analysis. Unsupervised machine learning methods have been used to automatically extract the different polar domain variants from the SHG anisotropy datacubes. The results obtained by machine learning methods were confirmed by the artisanal pixel-by-pixel analysis of the local SHG polar plots in the case of a thick film containing sufficiently large domains. Vertical and lateral piezoresponse force microscopy results further corroborate the SHG results. In addition to minimizing human intervention in the image analysis process and speeding up the data processing by avoiding the tedious pixel-by-pixel fitting procedure, the use of machine learning methods has allowed for resolving domain types in the

thinnest films that were not detectable by the human eye in conventional SHG analysis. This work shows that the application of advanced data processing methods assisted by machine learning increases the sensitivity and resolution of the optical method and allows for fast domain analysis.

## 2. Results and Discussion

Given the rhombohedral distortion and the existence of an electric dipole in the [111] direction in Germanium Telluride, eight possible polar domain orientations are expected in this system. This was unambiguously confirmed by the observation of heringbone domain configurations in bulk GeTe crystals.<sup>[19,20]</sup> The epitaxial growth of thin films on single crystal substrates often leads to the development of strain fields, providing an extra degree of freedom to control the domain structure. Various domain patterns can be obtained, depending on the balance between tensile or compressive epitaxial strain and the electrostatic and mechanic boundary conditions. Strain relaxation in thick epitaxial ferroelectric films is often accompanied by the formation of ferroelastic domains and twins showing a/c-domain boundaries with the main c-domain exhibiting out-of-plane polarization and fine a-domain incursions with in-plane polarization.<sup>[21–23]</sup> While such domain patterns have been intensively studied in the case of oxide perovskites, here, we show that similar multidomain structures can be observed in GeTe based on SHG microscopy and polarimetry analysis in combination with simulations based on the analytic form of SHG and symmetry arguments.

Even if SHG can probe nanoscale structures in particular cases owing to its quadratic sensitivity to local electric fields,<sup>[24]</sup> the lateral resolution of this nonlinear optical method is rather limited ( $\approx 300$  nm). Knowing that the size of the domains strongly decreases with the film thickness, the observation of the domain structure in thin ferroelectric films is therefore clearly challenging. A key solution to this challenge is provided by the application of machine learning that has been recently demonstrated as a pertinent approach for the investigation of ferroelectric materials.<sup>[25–30]</sup> Here, machine learning algorithms are applied to SHG data recorded for two different film thicknesses: a 1800 nm-thick GeTe film exhibiting 300 nm-wide stripe domains and a 200 nm-thick film showing 50 nm-wide stripe domains.

In the following, we first recall the basic principle of SHG polarimetry and its application to ferroelectric domain imaging. Then, a detailed artisanal analysis of the pixel-by-pixel SHG polarization response is presented for the 1800 nm-thick GeTe film. The SHG polar plots derived at each pixel are manually fitted using a complex analytic form of the SHG that accounts for both the light focusing effects and the mixed contribution of different domains in a given pixel. Given the fastidious and complex character of this task, different approaches are followed to simplify and automatize the analysis of the localized nonlinear optical response. We first use a simplified artisanal method that minimizes the effect of focusing as well as the multiple domain contributions by wisely selecting the measurement geometry. Finally, we test two analysis methods based on unsupervised machine learning for the automatic recognition of the domain variants in the thick GeTe film, containing 300 nm-wide domains, and in the thin GeTe film in which the domains' size is below the resolution limit of SHG.



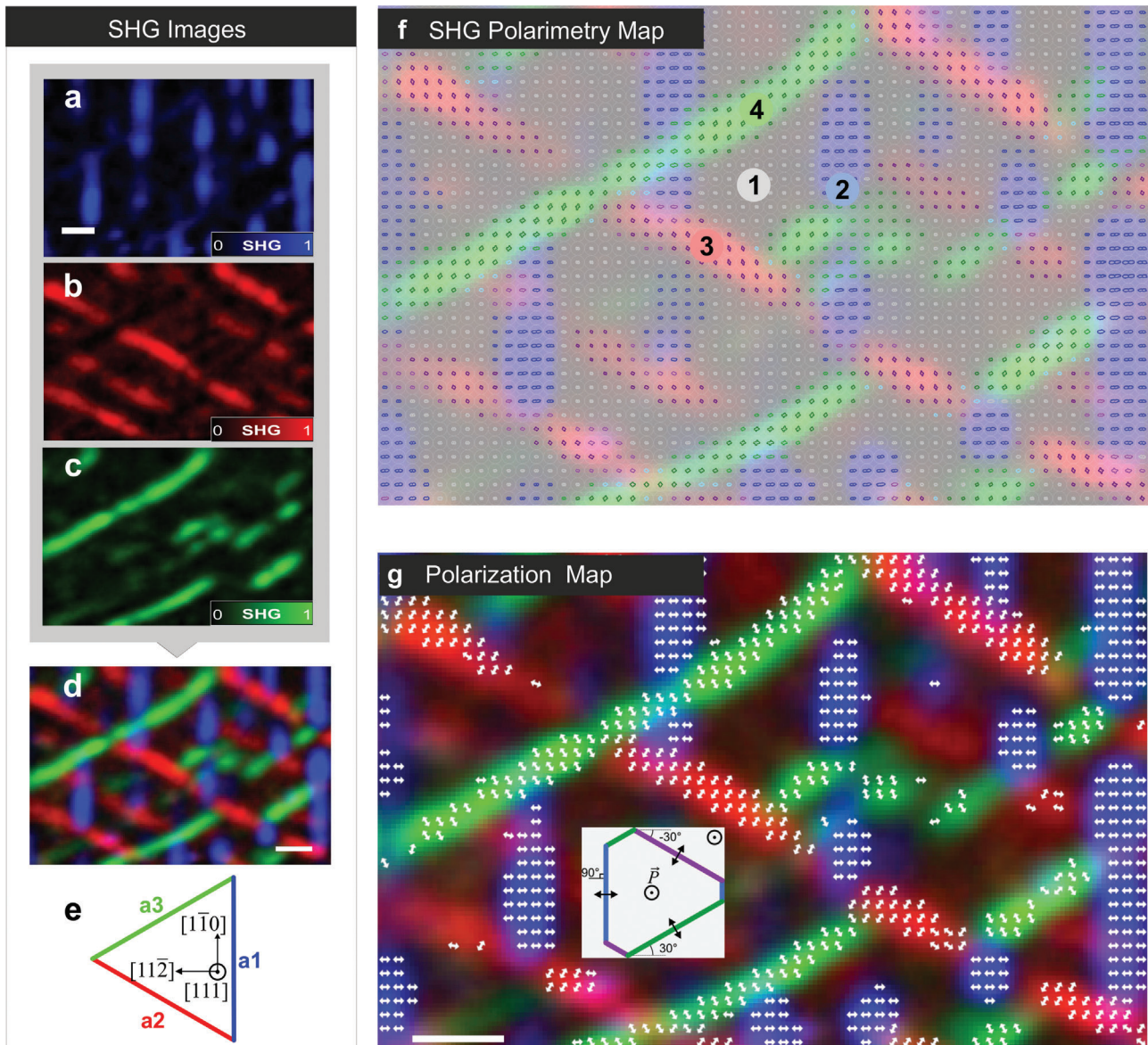


**Figure 1.** Revealing the domain structure of a 1800 nm-thick GeTe film by means of SHG microscopy with polarization analysis. SHG images were recorded at different sets of polarizer and analyzer angles allowing the observation of a)  $a_1$ -domains ( $\varphi = \alpha = 0^\circ$ ), b)  $a_1$ -domains ( $\varphi = \alpha = 60^\circ$ ), and c)  $a_3$ -domains ( $\varphi = \alpha = 120^\circ$ ). The resulting merged image displayed in panel (d) shows the three  $a$ -domains aligned along three different crystallographic orientations as depicted in panel (e), in addition to the main  $c$ -domain represented by the grey background. f) SHG polarimetry map showing the pixel-by-pixel SHG polarization response superimposed to the domain structure. Similar plots in terms of intensity and anisotropy are grouped, represented in a specific color code, and labeled 1, 2, 3, or 4. The fitting of the local polar plots at each pixel using the analytic form of SHG (Equation (7)) provides the polarization angle as an output parameter of the fit. A threshold  $R^2 = 0.90$  is set to select the best fitting results. In this case,  $>50\%$  of the selected results exhibit an  $R^2 > 0.96$ . g) The selected results of the fit are presented in the form of bidirectional arrows forming a polarization map that is superimposed on the SHG microscopy image. The scale bars are common to all images and correspond to  $2\ \mu\text{m}$ .

### 2.1. Revealing Polar Nanodomains by Means of Second-Harmonic Microscopy with Polarization Analysis

SHG microscopy has proven its efficiency in analyzing polarization states and symmetry aspects in various systems<sup>[31–33]</sup> among which: thermotropic phase boundaries,<sup>[34]</sup> phase coexistence in thin films<sup>[35]</sup> and heterostructures,<sup>[36]</sup> phase transitions,<sup>[37,38]</sup> non-Ising and chiral ferroelectric domain walls,<sup>[39,40]</sup> as well as polar domain boundaries in centrosymmetric materials.<sup>[41]</sup> The

variation of the SHG polarization with the light polarization provides a unique way to probe the nonlinear optical susceptibility tensor, and with this, to gain information on the local structure, symmetry, and polarization orientation in ferroelectric materials. SHG polarimetry measurements can consist of anisotropy plots (simultaneous rotation of the analyzer and polarizer, either parallel or perpendicular to each other), analyzer plots at a given incident light polarization, or by changing the incident light polarization and observing its effect on the second-harmonic emission

at a given analyzer angle. The SHG intensity variation with the incident laser polarization  $\varphi$  and analyzer angle  $\alpha$  is given by:

$$I^{SHG}(\varphi, \alpha) = |P^{2\omega}(\varphi, \alpha)|^2 = \sum_i |P_i(\varphi, \alpha)|^2 \quad (1)$$

The tensor form of the second-order polarization induced by the light-matter interaction  $P(\varphi, \alpha)$  reads:

$$\begin{pmatrix} P_x(\varphi) \\ P_y(\varphi) \\ P_z(\varphi) \end{pmatrix} = \epsilon_0 \begin{pmatrix} d_{11} & d_{12} & d_{13} & d_{14} & d_{15} & d_{16} \\ d_{21} & d_{22} & d_{23} & d_{24} & d_{25} & d_{26} \\ d_{31} & d_{32} & d_{33} & d_{34} & d_{35} & d_{36} \end{pmatrix} \begin{pmatrix} E_x^2(\varphi) \\ E_y^2(\varphi) \\ E_z^2(\varphi) \\ 2E_y E_z(\varphi) \\ 2E_x E_z(\varphi) \\ 2E_x E_y(\varphi) \end{pmatrix} \quad (2)$$

$$\begin{pmatrix} E_x^2 \\ E_y^2 \\ E_z^2 \\ 2E_x E_y \\ 2E_x E_z \\ 2E_y E_z \end{pmatrix} \approx \begin{pmatrix} \cos^2 \varphi \\ \sin^2 \varphi \\ -4I_1^2 \\ -4iI_1 \sin \varphi \cos \varphi \\ -4iI_1 \cos \varphi \cos \varphi \\ \sin(2\varphi) \end{pmatrix} \quad (6)$$

where  $E_i(\varphi)$  is the electric field of the fundamental wave, and  $d_{ij}$  represent the elements of the nonlinear optical susceptibility tensor written following the Voigt notation:  $2d_{ij} = \chi_{ikl}^{(2)}$ . The indices  $i, j, k$  refer to the Cartesian laboratory coordinates ( $x, y, z$ ). The complete dependence of the SHG response on the analyzer angle  $\alpha$  and the input polarization  $\varphi$  is obtained from Equation (2) using the Jones formalism accounting for the rotation  $\alpha$  of a linear polarizer as follows:

$$\begin{pmatrix} P_x(\varphi, \alpha) \\ P_y(\varphi, \alpha) \\ P_z(\varphi, \alpha) \end{pmatrix} = \begin{pmatrix} \cos^2 \alpha & \cos \alpha \sin \alpha & 0 \\ \cos \alpha \sin \alpha & \sin^2 \alpha & 0 \\ 0 & 0 & 1 \end{pmatrix} \begin{pmatrix} P_x(\varphi) \\ P_y(\varphi) \\ P_z(\varphi) \end{pmatrix} \quad (3)$$

GeTe films exhibit a trigonal symmetry 3m. The susceptibility tensor related to c-domains (polarization along the z-axis) can thus be written as

$$d^{c\text{-domains}} = \begin{pmatrix} 0 & 0 & 0 & 0 & d_{15} & -d_{22} \\ -d_{22} & d_{22} & 0 & d_{15} & 0 & 0 \\ d_{31} & d_{31} & d_{33} & 0 & 0 & 0 \end{pmatrix} \quad (4)$$

For a-domains with in-plane polarization oriented at an arbitrary angle  $\delta$  with respect to the  $x$ -axis in the laboratory coordinates system, the susceptibility tensor is derived using the rotation and transformation matrices as explained in Ref. [42]

$$d^{a\text{-domains}} = \begin{pmatrix} \sin \delta & 0 & \cos \delta \\ -\cos \delta & 0 & \sin \delta \\ 0 & -1 & 0 \end{pmatrix} \begin{pmatrix} 0 & 0 & 0 & 0 & d_{15} & -d_{22} \\ -d_{22} & d_{22} & 0 & d_{15} & 0 & 0 \\ d_{31} & d_{31} & d_{33} & 0 & 0 & 0 \end{pmatrix} \times \begin{pmatrix} \sin^2 \delta & \cos^2 \delta & 0 & 0 & 0 & -\sin 2\delta \\ 0 & 0 & 1 & 0 & 0 & 0 \\ \cos^2 \delta & \sin^2 \delta & 0 & 0 & 0 & \sin 2\delta \\ 0 & 0 & 0 & -\sin \delta & -\cos \delta & 0 \\ \frac{1}{2} \sin 2\delta & -\frac{1}{2} \sin 2\delta & 0 & 0 & 0 & -\cos 2\delta \\ 0 & 0 & 0 & \cos \delta & -\sin \delta & 0 \end{pmatrix} \quad (5)$$

In the case of a moderate focusing of the fundamental beam, which is the case when objectives of 0.70 numerical aperture (NA) or smaller are used, a scalar model of the electric field

$E(\varphi)$  based on the analytic form of SHG (Equations (1) and (2)) is sufficient to model the local polarimetry response in SHG experiments.<sup>[43]</sup> Spectromicroscopy, nevertheless, often requires high-resolution imaging and local spectroscopy analysis. An objective with 0.85 NA was, e.g., necessary to resolve the fine a-domains incursions in this study. In the case of focused light, the electric field in Equation (2) is written as<sup>[44]</sup>

where  $I_1$  is a focusing-related parameter ( $I_1 = 0.1$  for a 0.85 NA objective).<sup>[44]</sup> The scalar model, valid for unfocused photon beam or at optimum measurement geometry, is retrieved by taking  $I_1 = 0$ .

The domain structure of GeTe films is derived from SHG polarization analysis by fitting the local polar plots at each pixel using a semi-analytic model based on the analytic form of SHG. This is given by Equations (2), Equation (3), and by substituting the  $d_{ij}$  susceptibility tensor elements in Equation (3) by those of  $d^{c\text{-domains}}$  or  $d^{a\text{-domains}}$ . We also take into account the vector character of the electric field due to the tight focusing of the incident wave (substitution of the electric field given by Equation (6) in Equation (2)). The as-derived fitting function also considers the mixed a and c-domain fractions contributing to the SHG response. The mixed contribution is accounted for in the fit function using weighting factors  $W_a$  and  $W_c$  for a and c-domains, respectively, where  $W_a + W_c = 1$ . This leads to

$$I^{SHG} = W_c I_c^{SHG} + W_a I_a^{SHG} \quad (7)$$

where  $I_c^{SHG}$  and  $I_a^{SHG}$  represent the SHG response of the individual (pure) domains. The measurement geometry presented in Figure 1 allows for the detection of the four domain variants in a single anisotropy plot in which the analyzer and the polarizer are rotated simultaneously parallel to each other ( $\phi = \alpha$ ). In this case, the analytic form of the SHG responses is given by

$$I_c^{SHG} = D_1^2 \sin^2 3\alpha + 16I_1^2 \cos^2 \alpha \quad (8)$$

and

$$I_a^{SHG} = \left\{ \left[ (D_3 - D_2) \left( \cos^2(\alpha - \delta) + \frac{1}{2} \sin 2\delta \sin 2\alpha \right) + D_2 \right] \cos(\alpha - \delta) + \left( \sin 2(\alpha - \delta) + \frac{1}{2} \sin 2\delta \cos 2\alpha \right) \sin(\alpha - \delta) \right\}^2 + 16D_1^2 I_1^2 \cos^2 \alpha \left[ \cos \delta \cos(2\alpha - \delta) - \cos^2 \alpha \right]^2 \quad (9)$$

where the intrinsic anisotropy factors  $D_i$  correspond to the normalized nonlinear optical susceptibility factors  $D_1 = d_{22}/d_{15}$ ,  $D_2 = d_{31}/d_{15}$ ,  $D_3 = d_{33}/d_{15}$ .

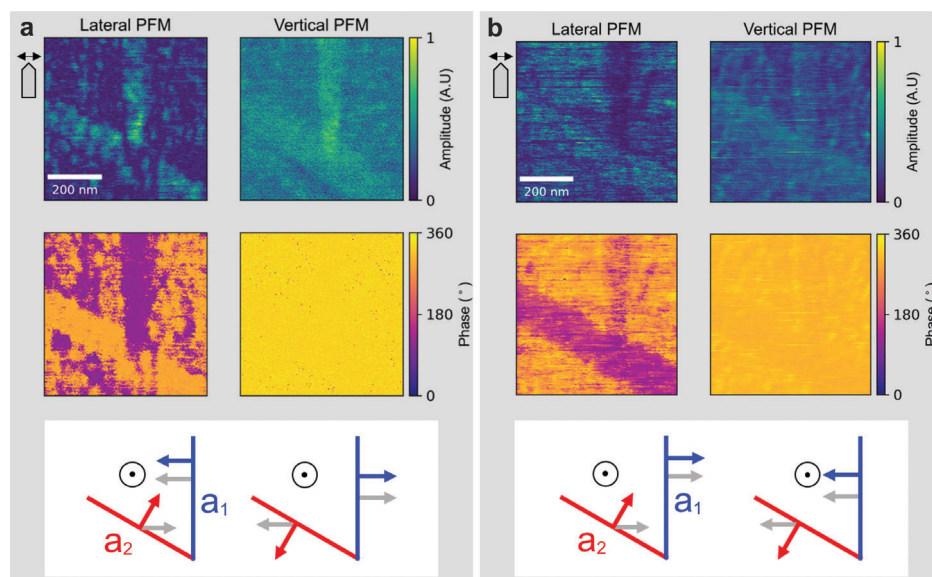


**Figure 2.** Vector piezoresponse force microscopy (PFM) measurements highlighting vertical and lateral responses in two different regions of a 1800 nm-thick GeTe grown on heavily-doped ( $\rho \approx 10^{-2} \Omega.cm$ ) Si(111) used as counter electrode. While vertical PFM shows a uniform phase contrast characteristic for out-of-plane polarization, lateral PFM shows in-plane polarization across the stripe domains in agreement with SHG results. It shows, furthermore, that the in-plane polarization in  $a_1$  and  $a_2$ -domains can be either in (a) opposite or in (b) the same direction with respect to each other, as schematically represented on the bottom part of each panel where the grey arrows represent the detected polarization component. The cantilever orientation during the measurements is shown on the left side of the two panels. The results obtained at different cantilever-sample rotation angles are given in Figure S1 (Supporting Information).

### 2.1.1. Manual Data Processing Method

In practice, local SHG polarimetry analysis is conducted by recording a set of images as a function of the polarizer and analyzer angles. In this study, local anisotropy plots were obtained by the simultaneous rotation of the polarizer and analyzer while keeping them parallel to each other leading to the so-called SHG anisotropy plots. The images of the recorded stack are subdivided into a checkerboard consisting of homogeneous squares of multiple pixels (typically  $3 \times 3$  pixels<sup>2</sup>). A polar plot is derived at each superpixel by integrating the local SHG intensity over the stack of images. These plots are then represented at their superpixel center position to form a polar plot map as displayed in Figure 1e. The fitting of each local polar plot provides the polarization angle as an output fit parameter. A bidirectional arrow with a given orientation can, thus, be assigned to each superpixel. This results in a polarization map that can be superimposed on the SHG microscopy image (Figure 1d) for better clarity as shown in Figure 1f. This conventional analysis method that we refer to as the artisanal method shows the existence of four domain variants in the 1800 nm-thick GeTe films. The main domain exhibits an out-of-plane polarization (c-domain), and the three additional stripe domains ( $a_{1,2,3}$ -domains) exhibit in-plane polarization along the short axis of the stripe (see Figure 1g inset).

From vector piezoresponse force microscopy (PFM) measurements carried out on the 1800 nm-thick GeTe sample, we can confirm that the out-of-plane polarization of the c-domain is uniform throughout the film, with no phase contrast visible in vertical PFM measurements. The lateral PFM measurements, meanwhile, show a distinct phase signal at the twin domains, corresponding to a polarization oriented across the width of the stripe

domain, in agreement with SHG results. From measurements at different cantilever-sample rotation angles (see Figure S1 and the related text in the Supporting Information), we can obtain a full picture of the polar axis assignments in these structures. The two sample regions presented in **Figure 2** show that  $a_1$  and  $a_2$  twin domains can present either identical or reversed contrasts with respect to each other, corresponding to a parallel or anti-parallel polarization orientation of the in-plane components.

### 2.1.2. Minimising the Effects of Mixed Domain Contributions and SHG Polarimetry Distortions Due to Focusing

Additional polarimetry measurements are performed by recording the variation of the second-harmonic response as a function of the analyzer angle at a fixed incident light polarization  $\varphi = 90^\circ$ . These measurements are repeated three times such that the stripe domains  $a_1$ ,  $a_2$ , and  $a_3$  are aligned with the  $x$ -axis in each measurement. In this configuration, the SHG signal arises mainly from horizontally aligned domains (i.e., parallel to  $x$ -axis), thereby minimizing the mixed contributions of the c-domain and the two other a-domains. In addition, this geometry is expected to reduce the effects of the light focusing and, thus, obtain distortion-free polar plots in a similar way as demonstrated in the case of non-Ising domains presenting in-plane polarization.<sup>[44]</sup>

**Figure 3** shows that the second-harmonic responses of the three a-domains show the same uniaxial anisotropy with a maximum intensity along the short axis of the stripe domains. This result indicates that the three stripe domains share the same nature and polarization orientation. The polar plots obtained



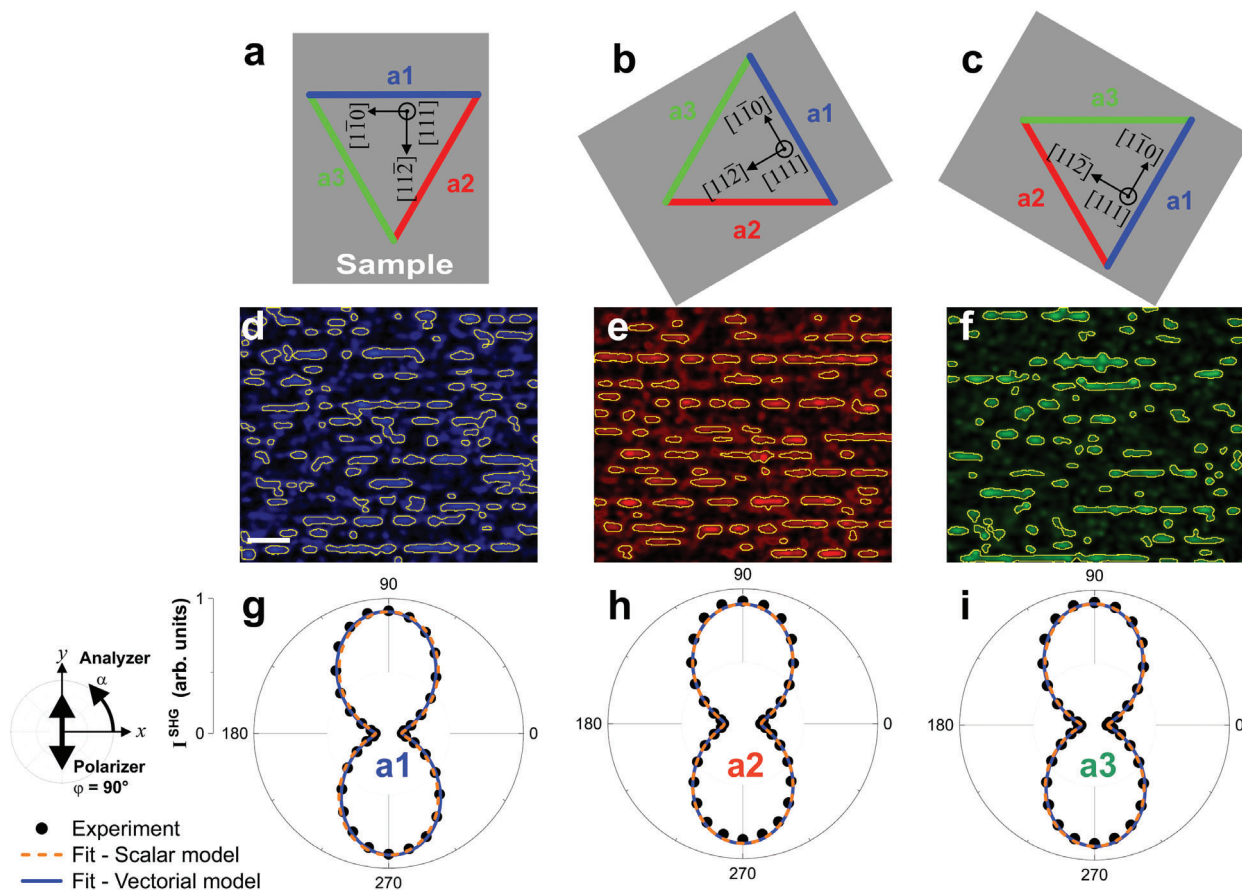


**Figure 3.** Geometry-dependent SHG polarimetry analysis. The sample azimuth angle is rotated by a)  $90^\circ$ , b)  $+30^\circ$ , and c)  $-30^\circ$  so that each stripe domain ( $a_1$ ,  $a_2$ ,  $a_3$ ) is aligned with the  $x$ -axis during the measurements. SHG microscopy images showing d)  $a_1$ -domains, e)  $a_2$ -domains, and f)  $a_3$ -domains. These images are measured at  $\varphi = \alpha = 90^\circ$ . The scale bar shown in panel (b) represents  $2\ \mu\text{m}$  and is common to the three images. SHG polar plots ( $\alpha$ -plots) have been conducted at a fixed input polarization angle  $\varphi = 90^\circ$  in the three sample configurations displayed in panels (a), (b), and (c), allowing the specific probe of g)  $a_1$ , h)  $a_2$ , and i)  $a_3$ -domain components, respectively while minimizing the distortion of the polar plots due to focusing effects.<sup>[44]</sup> The experimental polar plots are represented by scattered dots, while the fit results are presented in blue continuous lines (scalar model) and orange dashed lines (vectorial model).

for  $a_1$ ,  $a_2$ , and  $a_3$  domains (dots in Figure 3g–i) are perfectly fitted using the vectorial (blue continuous line) and scalar (red dashed line) models of SHG. The fits show that the polarization is along the short axis of the stripes. The perfect overlap of the curves obtained by the two fit models confirms that this measurement geometry reduces focusing effects, in the same way as in non-Ising domain walls.<sup>[44]</sup>

It is worth noting that in these measurement configurations, the modeling and interpretation of the results are highly simplified with respect to the method presented in the previous section. Yet, obtaining complete information on the domain structure requires a large number of measurements at different sample orientations to properly probe each domain variant.

## 2.2. Machine Learning-Assisted Second-Harmonic Generation Polarimetry Analysis

In the following subsections, we will demonstrate that machine-learning-assisted analysis of the data resulting from a single

measurement geometry can be sufficient to easily retrieve the domain structure. The complete analysis workflow presented in this study is implemented using the Python 3 programming language. The program contains a code to load and pre-process the SHG data cube (stack of images recorded at different polarizer and analyzer angles), as well as the K-means clustering and non-negative matrix factorization codes implemented via open access Python packages.<sup>[45]</sup>

### 2.2.1. Deriving the Domain Structure Using the K-Means Clustering Method

Ferroelectric thin films and superlattices develop complex domain configurations and topological structures. For example, in GeTe thin films, several variants and intricate domain patterns are expected. Human perception may not be sufficient to reach a precise segmentation of the SHG polarimetry data in an unbiased manner. Machine-learning-based techniques have recently proven their efficiency in such cases. In particular, clustering

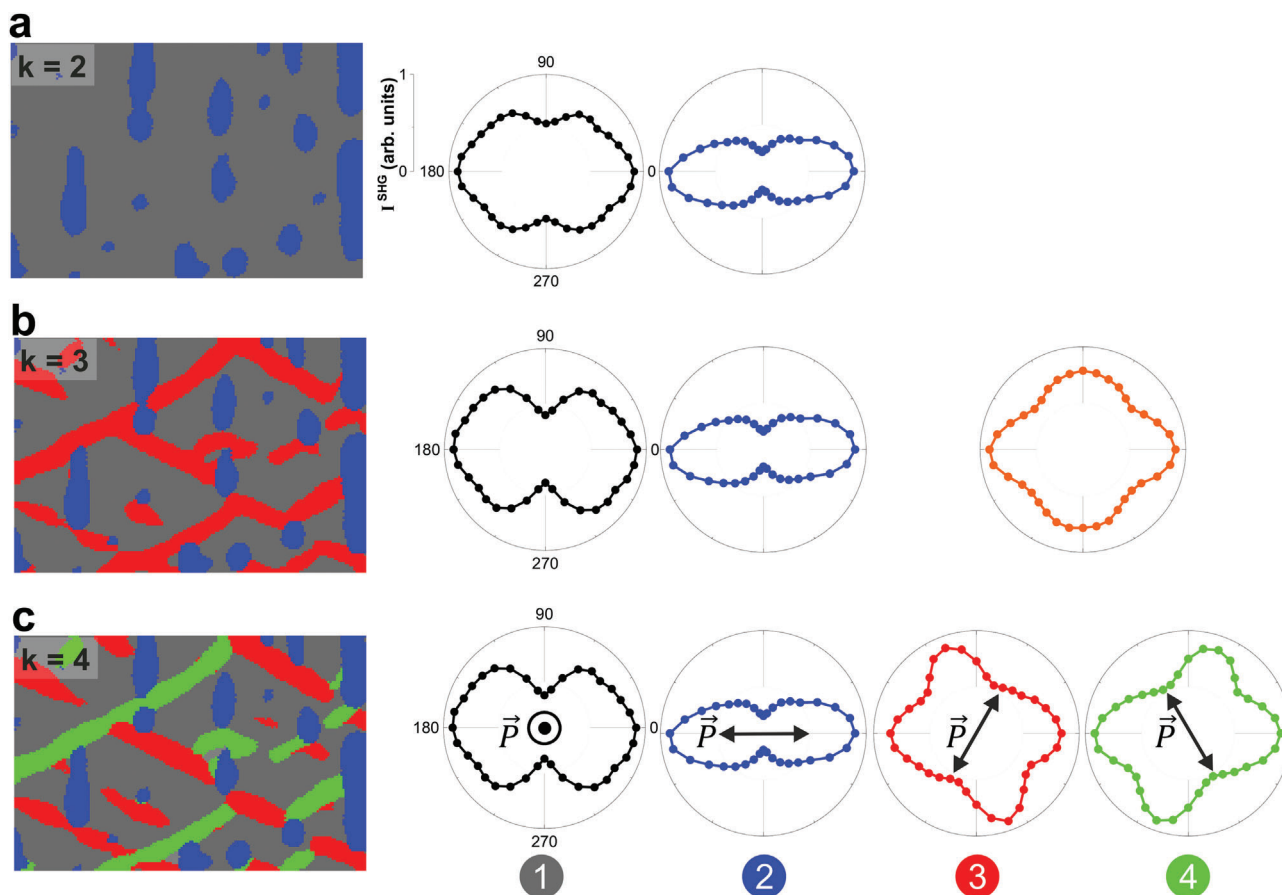


**Figure 4.** K-means clustering applied to SHG polarimetry analysis. The method is applied to SHG anisotropy plots (polarizer rotating parallel to the analyzer) measured in a 1800 nm-thick GeTe film area of  $15 \times 10^{-4} \mu\text{m}^2$ . As the number of clusters increases, more domains are resolved. Each image represents the spatial distribution of the clusters (i.e., the ferroelectric domains) identified by a colored region and their corresponding polar plots presented in the same color code. a) Two clusters ( $k = 2$ ) containing the background (gray) and vertical stripe domains (blue). b) Three clusters ( $k = 3$ ) including the background (gray) and the vertical stripe domains (blue), in addition to oblique stripe domains with positive or negative tilt angles (red). c) Four clusters ( $k = 4$ ) in which the two oblique domains that were indistinguishable in panel (b) could be identified by individual clusters (green and red) depending on their orientation. The polar plot contributions corresponding to the four domain variants identified by the K-means method are fitted using the complex analytic form of SHG accounting for focusing effects and mixed domain contributions. The resulting polarization orientations are superimposed on the polar plots in panel (c).

methods are highly suited for the identification of groups with distinct properties in a given data set, based on a concept of similarity between elements within each cluster.<sup>[15,30,46,47]</sup> In the present analysis, clustering was performed through K-means clustering in order to segment the SHG datasets into regions of interest with distinct behaviors corresponding to ferroelectric domain variants. Euclidean distance criterion is used to segment the data set into spatially indexed clusters, with centroids encoding the differing mean behaviors within each cluster. The algorithm is then initialized with  $k$  randomly distributed centroids, and each point is attributed to the cluster of the closest centroid. The centroids are then displaced to the resulting cluster center. This expectation-maximization process is repeated until convergence, with the cluster number for each parameter space vector assigned to its spatial position. When applied to polarization-dependent SHG microscopy measurements, the K-means clustering method tends to find the shortest distances

between the measured polar plots and the centroids. At the end of the iterations, we obtain centroids corresponding to the typical average polar plots contained in the system, and different clusters corresponding to the domains linked to a given polar plot type as detailed in Figure S2 and the related text in the Supporting Information.

The K-means analysis of the SHG polarimetry data set related to the 1800 nm-thick GeTe film is shown in **Figure 4** for a number of clusters ranging from  $k = 2$  to  $k = 4$ . At the lowest cluster count,  $k = 2$ , the resulting map displays two color-coded clusters: one containing the main c-domain (grey background in Figure 4), and the other representing the vertical a-stripe domains (blues vertical stripes Figure 4). Increasing the number of clusters  $k$  has the effect of identifying a larger number of regions with a distinct SHG signal, thus revealing additional domain variants. Having four clusters  $k = 4$  yield a cluster distribution that corresponds to those identified by eye in the



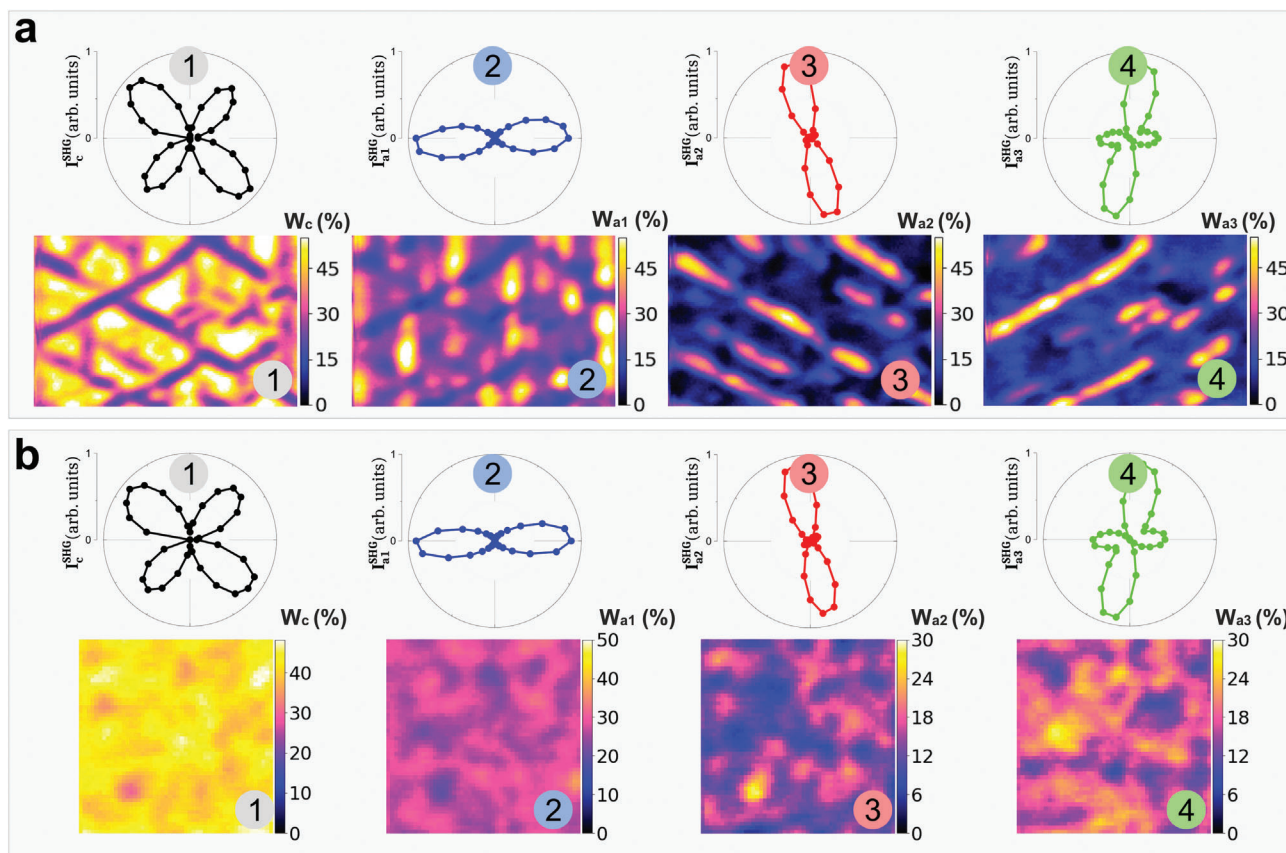


**Figure 5.** Application on Non-negative Matrix Factorization (NMF) method to laterally-resolved SHG polarimetry data. The NMF method is applied to SHG anisotropy plots (polarizer rotating parallel to the analyzer) measured in a) 1800 nm-thick GeTe film area of  $15 \times 10^{-6} \mu\text{m}^2$ , and b) 200 nm-thick GeTe film area of  $10 \times 10^{-6} \mu\text{m}^2$ . The polar plots labeled 1, 2, 3, and 4 in each panel correspond to the four polar plot types (centroids) detected in a given film thickness. The images displayed beneath each polar plot correspond to the contribution of each polar plot type to the SHG image. The as-derived SHG polarimetry maps correspond to the four domain variant fractions  $W_c$ ,  $W_{a_1}$ ,  $W_{a_2}$ , and  $W_{a_3}$  at each pixel.

artisanal approach detailed above. The four clusters formed by the main c-domain (gray, corresponding to the polar plot labeled 1 in Figure 4), the vertical  $a_1$ -domain (blue, corresponding to the polar plot labeled 2 in Figure 4), and the two oblique  $a_2$  (red, corresponding to the polar plot labeled 3 in Figure 4) and  $a_3$ -domains (green, corresponding to the polar plot labeled 4 in Figure 4) are fully recovered, without requiring any manual input except the number of clusters. The K-means method takes only a few seconds (2.5 s) to retrieve the domain variants present in the system, while the pixel-by-pixel polarimetry analysis leading to polarization maps such as that presented in Figure 1g can take up to 48 h. Nonetheless, the main drawback of the K-means approach is the association of polar plots to a single cluster even if they exhibit slightly different behaviors.<sup>[29]</sup> Therefore, small or gradual polarization variations from one pixel to the other are washed-out by the K-means method. Besides, in the case of different coexisting domains of small sizes such as those expected for 200 nm-thin GeTe exhibiting (sub-100 nm domains), the K-means method fails (see Figure S3, Supporting Information). The use of more advanced dimensional reduction techniques such as the non-negative matrix factorization method that we discuss below could be applied in these challenging cases to enable intermixed behaviors to be separated.

### 2.2.2. Improving the Sensitivity to Nanodomains Using Non-negative Matrix Factorization

Non-negative Matrix Factorization (NMF) is an algorithm that factorizes an input matrix into two matrices. In the case of laterally-resolved SHG polarimetry, the input matrix is the polarimetry data cube and the two output matrices are the SHG polar plots, and the fraction of each polar plot at a given pixel (see Figure S4 and the related text in the Supporting Information). This method is particularly suited for SHG data analysis since it assumes non-negative matrix elements corresponding to a non-negative SHG intensity. Besides, owing to its decomposition procedure, the NMF method is particularly adapted to the study of mixed signals per pixel, such as the mixed a/c-domain contribution to the SHG signal in the case of GeTe films. It is also worth noting this method provides the 2D distribution of the polar plot fractions (i.e., a given polar plot type percentage per pixel), while the K-means method shows the presence or absence of a given polar plot type (cluster). We, therefore, represent the NMF results in a different color code.

The NMF method was first tested in the case of the 1800 nm-thick GeTe film so that the results can be compared to those obtained by the artisanal and K-means methods. This method

provides the contribution to the SHG intensity of each domain type at each pixel, as displayed in **Figure 5a**. Four domain fractions  $W_c$ ,  $W_{a_1}$ ,  $W_{a_2}$ , and  $W_{a_3}$  have been derived in this case, in agreement with the results obtained by the K-mean method (Figure 4) as well as those obtained by the artisanal method (Figure 1). The polar plots derived by the NMF method correspond to those obtained by the K-means method after the subtraction of the mean intensity per image (see Figure S5, Supporting Information).

Let now apply the NMF method to the SHG data obtained for a 200 nm-thick GeTe in which both the human eye and the K-mean method fail to resolve the 50 nm wide stripe domains. In this sample, there is a low proportion of domains thus their signature is faint and their lateral size is far lower than the resolution of the SHG microscope (300 nm). Figure 5b shows that four different domain contributions could be extracted with the NMF algorithm showing similar signatures as those obtained in the case of the 1800 nm-thick film. These results were obtained by using the centroids derived from the K-means method in the 1800 nm-thick GeTe film as initialization parameters. The SHG polarimetry maps displayed in Figure 5 are derived by using 70 % c-domain and 10 % for  $a_1$ ,  $a_2$ , and  $a_3$ -domain variants as initial parameters. The c/a-domain fractions are in the range of the experimentally derived values by means of 3D X-ray diffraction reciprocal space mapping.<sup>[48]</sup> The robustness of the NMF results was assessed by testing several parameters and initialization conditions. As shown in the Supporting Information (see Figure S6 and the related text in the Supporting Information), the results derived by the NMF method are independent of the initial conditions used for the calculations.

### 3. Conclusion

In summary, we analyzed the domain structure of GeTe ferroelectric epitaxial films using nonlinear optical microscopy with spatially-resolved polarization analysis. The conventional, manual method requires a pixel-by-pixel analysis of the SHG polarimetry data and the fitting of more than 2000 polar plots using a complex analytic form of the second-harmonic emission accounting for both the light focusing effect and the mixed contribution of the domains at each pixel. Different approaches are followed to simplify and automatize the determination of the domain structure based on the localized nonlinear optical responses. In particular, we show how suitable data analysis supported by machine learning methods enables a fast and reliable automatic determination of the domain variants and their typical polarimetry signature. K-means clustering identified four domain contributions in the 1800 nm-thick GeTe film, in agreement with the artisanal method. The NMF method confirmed this result and revealed the same number and type of domain variants in the 200 nm-thin GeTe film containing nanodomains that could not be resolved by the human eye nor detected by K-means clustering. The approach developed in this study foreshows new prospects for nonlinear optical microscopy studies by enabling enhanced sensitivity and high throughput analysis, following the steps of recent advances in scanning probe microscopy.<sup>[46,49,50]</sup> It can be applied not only to the study of functional materials, such as ferroelectrics, but also to, e.g.,

the automatic detection of SHG polarimetry signatures related to diseased cells in biomedical science.

### 4. Experimental Section

**Materials:** The ferroelectric  $\alpha$ -GeTe films examined in this study were epitaxially grown by means of molecular beam epitaxy on Si(111) wafers. The Si(111) substrate was first cleaned with acetone and ethanol and then transferred into the ultra-high vacuum. The substrate was first out-gassed for several hours at 700°C, then flashed at 1200°C to obtain a clean Si(111) surface showing typical Si(111)-7 $\times$ 7 surface reconstruction. An atomic layer of antimony was deposited as a buffer layer to improve the crystalline quality of the GeTe film. single crystalline GeTe films were subsequently grown at 275°C by co-depositing germanium and tellurium. GeTe showed a BiFeO<sub>3</sub>-like structure with a rhombohedral distortion and a related electric dipole along the [111] direction. While eight possible polar domain orientations could be anticipated in that system, the epitaxial strain imposed by the growth on Si(111) led to reduced domain variants and the development of complex domain patterns including three polar distortions along  $[1\bar{1}\bar{1}]$ ,  $[1\bar{1}\bar{1}]$  and  $[\bar{1}11]$ , in addition to the main ferroelectric domain oriented along the film thickness [111]. That resulted in a polydomain structure with the main c-domain containing fine elastic stripe domain incursions oriented in three different directions. More details about the growth conditions and the evolution of the domain structure depending on the thermal kinetics can be found in Ref. [48].

**Second-Harmonic Generation Microscopy:** Local SHG measurements were conducted in an inverted optical microscope. The fundamental wave was provided by a laser source emitting pulses of 100 fs duration at a repetition rate of 80 MHz, centered at a wavelength  $\lambda = 800$  nm. The sample was illuminated at normal incidence with a time-averaged power of  $\approx 10$  mW. The SHG images were obtained by scanning the sample with respect to the focused laser beam (objective  $\times 60$ , 0.85 numerical aperture) using computer-controlled stepping motors. The output intensity was spectrally filtered and collected into a photomultiplier. Polarimetry measurements were performed by recording the SHG images at different polarizer, and analyzer angles ( $\varphi$  and  $\alpha$ , respectively). Ref. [42] provides detailed information on the measurement geometry.

**Piezoresponse Force Microscopy:** The scanning probe microscopy imaging were carried out using an Asylum Research Cypher ES atomic force microscope, equipped with an in-house-built flow-based, low noise humidity controller, to have a dry controlled atmosphere, and the sample temperature was kept constant at 30°C. In this way, the role of adsorbates on the surface is lessened. The piezoresponse force microscopy (PFM) measurements were acquired in single-frequency Vector PFM mode, acquiring the in-plane and the out-of-plane signal simultaneously, using ASYLEC-R1 cantilevers with a resonance frequency of 75 kHz and a spring constant of  $\approx 2$  nN nm<sup>-1</sup>.

### Supporting Information

Supporting Information is available from the Wiley Online Library or from the author.

### Acknowledgements

This work was supported by the French National Research Agency (ANR) under contract No. ANR-18-CE92-0052 and ANR-22-CE08-0023. We acknowledge the Interdisciplinary Thematic Institute EUR QMat (ANR-17-EURE-0024), as part of the ITI 2021-2028 program supported by the IdEx Unistra (ANR-10-IDEX-0002) and SFRI STRAT'US (ANR-20-SFRI-0012) through the French Programme d'Investissement d'Avenir.

### Conflict of Interest

The authors declare no conflict of interest.

## Data Availability Statement

The data that support the findings of this study are available from the corresponding author upon reasonable request.

## Keywords

clustering methods, domains, ferroelectrics, GeTe, machine learning, non-negative matrix factorization, second-harmonic generation

Received: September 10, 2022

Revised: October 30, 2022

Published online:

- [1] A. K. Tagantsev, L. E. Cross, J. Fousek, *Domains in Ferroic Crystals and Thin Films*, 1 ed., Springer, New York **2010**.
- [2] P. Ferraro, S. Grilli, P. De Natale), *Ferroelectric Crystals for Photonic Applications*, 1 ed., vol. 91, Springer Series in Materials Science, Springer Berlin Heidelberg, Berlin, Heidelberg **2009**.
- [3] D. Meier, J. Seidel, M. Gregg, R. Ramesh, *Domain Walls*, Oxford University Press, Oxford **2020**.
- [4] A. K. Yadav, C. T. Nelson, S. L. Hsu, Z. Hong, J. D. Clarkson, C. M. Schlepütz, A. R. Damodaran, P. Shafer, E. Arenholz, L. R. Dedon, D. Chen, A. Vishwanath, A. M. Minor, L. Q. Chen, J. F. Scott, L. W. Martin, R. Ramesh, F.-H. Gong, Y.-L. Tang, Y.-L. Zhu, H. Zhang, Y.-J. Wang, Y.-T. Chen, Y.-P. Feng, M.-J. Zou, B. Wu, W.-R. Geng, Y. Cao, X.-L. Ma, *Nature* **2016**, 530, 198.
- [5] D. Rusu, J. J. P. Peters, T. P. A. Hase, J. A. Gott, G. A. A. Nisbet, J. Stremper, D. Haskell, S. D. Seddon, R. Beanland, A. M. Sanchez, M. Alexe, *Nature* **2022**, 602, 240.
- [6] F. H. Gong, Y. L. Tang, Y. L. Zhu, H. Zhang, Y. J. Wang, Y. T. Chen, Y. P. Feng, M. J. Zou, B. Wu, W. R. Geng, Y. Cao, X. L. Ma, *Sci. Adv.* **2021**, 7, 28.
- [7] S. Fusil, J. Y. Chauleau, X. Li, J. Fischer, P. Dufour, C. Léveillé, C. Carrière, N. Jaouen, M. Viret, A. Gloter, V. Garcia, *Adv. Electron. Mater.* **2022**, 8, 1.
- [8] A. Gruverman, M. Alexe, D. Meier, *Nat. Commun.* **2019**, 10, 1661.
- [9] L. M. Eng, H.-J. Güntherodt, G. A. Schneider, U. Köpke, J. Muñoz Saldaña, *Appl. Phys. Lett.* **1999**, 74, 233.
- [10] S. Cherifi, R. Hertel, S. Fusil, H. Béa, K. Bouzouane, J. Allibe, M. Bibes, A. Barthélémy, *physica status solidi (RRL) - Rapid Research Letters* **2010**, 4, 22.
- [11] G. F. Nataf, N. Barrett, J. Kreisel, M. Guennou, *J. Phys.: Condens. Matter* **2018**, 30, 035902.
- [12] F. Lussier, V. Thibault, B. Charron, G. Q. Wallace, J.-F. Masson, *TrAC Trends in Analytical Chemistry* **2020**, 124, 115796.
- [13] W. Fan, T. Chen, E. Gil, S. Zhu, V. Yakovlev, D.-W. Wang, D. Zhang, *ACS Photonics* **2021**, 8, 1562.
- [14] K. Mirsanaye, L. Uribe Castaño, Y. Kamaliddin, A. Golaraei, R. Augulis, L. Kontenis, S. J. Done, E. Žurauskas, V. Stambolic, B. C. Wilson, V. Barzda, *Sci. Rep.* **2022**, 12, 10290.
- [15] I. Gaponenko, S. Cherifi-Hertel, U. Acevedo-Salas, N. Bassiri-Gharb, P. Paruch, *Sci. Rep.* **2022**, 12, 165.
- [16] D. D. Sante, P. Barone, R. Bertacco, S. Picozzi, *Adv. Mater.* **2012**, 25, 509.
- [17] S. Datta, *Nat. Electron.* **2018**, 1, 604.
- [18] S. Varotto, L. Nesi, S. Cecchi, J. Sławińska, P. Noël, S. Petrò, F. Fagiani, A. Novati, M. Cantoni, D. Petti, E. Albisetti, M. Costa, R. Calarco, M. B. Nardelli, M. Bibes, S. Picozzi, J.-P. Attané, L. Vila, R. Bertacco, C. Rinaldi, *Nat. Electron.* **2021**, 4, 740.
- [19] H. S. Lee, B. S. Kim, C. W. Cho, M. W. Oh, B. K. Min, S. D. Park, H. W. Lee, *Acta Materialia* **2015**, 91, 83.
- [20] P. A. Vermeulen, A. Kumar, G. H. Ten Brink, G. R. Blake, B. J. Kooi, *Crystal Growth and Design* **2016**, 16, 10.
- [21] V. Nagarajan, I. G. Jenkins, S. P. Alpay, H. Li, S. Aggarwal, L. Salamanca-Riba, A. L. Roytburd, R. Ramesh, *J. Appl. Phys.* **1999**, 86, 595.
- [22] A. H. Vlooswijk, B. Noheda, G. Catalan, A. Janssens, B. Barcones, G. Rijnders, D. H. Blank, S. Venkatesan, B. Kooi, J. T. De Hosson, *Appl. Phys. Lett.* **2007**, 91, 20.
- [23] L. Feigl, L. J. McGilly, C. S. Sandu, N. Setter, *Appl. Phys. Lett.* **2014**, 104, 172904.
- [24] L. Bonacina, P.-F. Brevet, M. Finazzi, M. Celebrano, *J. Appl. Phys.* **2020**, 127, 230901.
- [25] R. K. Vasudevan, S. Zhang, M. Baris Okatan, S. Jesse, S. V. Kalinin, N. Bassiri-Gharb, *J. Appl. Phys.* **2015**, 118, 072003.
- [26] L. Li, Y. Yang, D. Zhang, Z.-G. Ye, S. Jesse, S. V. Kalinin, R. K. Vasudevan, *Sci. Adv.* **2018**, 4, eaap8672.
- [27] S. M. Neumayer, S. Jesse, G. Velarde, A. L. Kholkin, I. Kravchenko, L. W. Martin, N. Balke, P. Maksymovych, *Nanoscale Advances* **2020**, 2, 2063.
- [28] R. K. Vasudevan, K. Choudhary, A. Mehta, R. Smith, G. Kusne, F. Tavazza, L. Vlcek, M. Ziatdinov, S. V. Kalinin, J. Hattrick-Simpers, *MRS Communications* **2019**, 9, 821.
- [29] L. A. Griffin, I. Gaponenko, N. Bassiri-Gharb, *Adv. Mater.* **2020**, 32, 2002425.
- [30] F. Zhang, K. N. Williams, D. Edwards, A. B. Naden, Y. Yao, S. M. Neumayer, A. Kumar, B. J. Rodriguez, N. Bassiri-Gharb, *Small Methods* **2021**, 5, 2100552.
- [31] H. Yokota, J. Kaneshiro, Y. Uesu, *Physics Research International* **2012**, 2012, 1.
- [32] S. A. Denev, T. T. A. Lummen, E. Barnes, A. Kumar, V. Gopalan, *J. Am. Ceram. Soc.* **2011**, 94, 2699.
- [33] M. Trassin, G. D. Luca, S. Manz, M. Fiebig, *Adv. Mater.* **2015**, 27, 4871.
- [34] T. T. Lummen, Y. Gu, J. Wang, S. Lei, F. Xue, A. Kumar, A. T. Barnes, E. Barnes, S. Denev, A. Belianinov, M. Holt, A. N. Morozovska, S. V. Kalinin, L.-Q. Chen, V. Gopalan, *Nat. Commun.* **2014**, 5, 3172.
- [35] A. Kumar, S. Denev, R. J. Zeches, E. Vlahos, N. J. Podraza, A. Melville, D. G. Schlom, R. Ramesh, V. Gopalan, *Appl. Phys. Lett.* **2010**, 97, 112903.
- [36] N. Strkalj, A. Bortis, M. Campanini, M. D. Rossell, M. Fiebig, M. Trassin, *Phys. Rev. B* **2022**, 105, 174101.
- [37] V. Gopalan, R. Raj, *Appl. Phys. Lett.* **1996**, 68, 1323.
- [38] W. Li, Y. Ma, T. Feng, S. V. Kalinin, J.-F. Li, Q. Li, Delineating complex ferroelectric domain structures via second harmonic generation spectral imaging, **2022**, <https://arxiv.org/abs/2208.04540>
- [39] S. Cherifi-Hertel, H. Bulou, R. Hertel, G. Taupier, K. D. Dorkenoo, C. Andreas, J. Guyonnet, I. Gaponenko, K. Gallo, P. Paruch, *Nat. Commun.* **2017**, 8, 15768.
- [40] U. Acevedo-Salas, B. Croes, Y. Zhang, O. Cregut, K. D. Dorkenoo, B. Kirbus, E. Singh, H. Beccard, M. Rüsing, L. M. Eng, R. Hertel, E. A. Eliseev, A. N. Morozovska, S. Cherifi-Hertel, Impact of 3d curvature on the polarization orientation in non-ising domain walls, **2022**, <https://arxiv.org/abs/2207.01307>.
- [41] H. Yokota, Y. Uesu, *J. Appl. Phys.* **2021**, 129, 014101.
- [42] S. Cherifi-Hertel, C. Voulot, U. Acevedo-Salas, Y. Zhang, O. Cregut, K. D. Dorkenoo, R. Hertel, *J. Appl. Phys.* **2021**, 129, 081101.
- [43] M. Gu, *Advanced Optical Imaging Theory*, vol. 75, Springer Series in Optical Sciences, Springer Berlin Heidelberg, Berlin, Heidelberg **2000**.
- [44] Y. Zhang, S. Cherifi-Hertel, *Opt. Mater. Express* **2021**, 11, 3736.
- [45] F. Pedregosa, G. Varoquaux, A. Gramfort, V. Michel, B. Thirion, O. Grisel, M. Blondel, P. Prettenhofer, R. Weiss, V. Dubourg, J. Vanderplas, A. Passos, D. Cournapeau, M. Brucher, M. Perrot, Édouard Duchesnay, *Journal of Machine Learning Research* **2011**, 12, 2825.



- [46] S. W. Schmitt, R. K. Vasudevan, M. Seifert, A. Y. Borisevich, V. Deshpande, S. V. Kalinin, C. Dubourdieu, *ACS Applied Electronic Materials* **2021**, *3*, 4409.
- [47] Y. Hiranaga, T. Mimura, T. Shimizu, H. Funakubo, Y. Cho, *Jpn. J. Appl. Phys.* **2022**, *61*, SN1014.
- [48] B. Croes, F. Cheynis, Y. Zhang, C. Voulot, K. D. Dorkenoo, S. Cherifi-Hertel, C. Mocuta, M. Texier, T. Cornelius, O. Thomas, M.-I. Richard, P. Müller, S. Curiotto, F. Leroy, *Phys. Rev. Materials* **2021**, *5*, 124415.
- [49] M. Ziatdinov, D. Kim, S. Neumayer, L. Collins, M. Ahmadi, R. K. Vasudevan, S. Jesse, M. H. Ann, J. H. Kim, S. V. Kalinin, *J. Appl. Phys.* **2020**, *128*, 055101.
- [50] Y. Liu, K. P. Kelley, H. Funakubo, S. V. Kalinin, M. Ziatdinov, *Adv. Sci.* **2022**, *9*, 2203957.